STRUCTURAL EVOLUTION OF α-Fe_2O_3 NANOWIRES DURING LITHIATION/DELITHIATION AND ELECTROCHEMICAL PROPERTY IMPROVEMENT

BY

BO HUANG

THESIS

Submitted in partial fulfillment of the requirements
for the degree of Master of Science in Materials Science and Engineering
in the Graduate College of the
University of Illinois at Urbana-Champaign, 2013

Urbana, Illinois

Adviser:

Assistant Professor Shen J. Dillon

ABSTRACT

Hematite Fe_2O_3 exhibits great potential in lithium ion battery area as anode material, due to high capacity, elemental abundance, low cost and biocompatibility. Its reaction with lithium ion is accepted as conversion reaction. In this paper, single crystal α-Fe_2O_3 nanowires were prepared by an electrical resistive heating method under ambient conditions. Transmission electron microscopy characterized the anode material at various stages of lithiation and delithiation. The phase and morphological evolution demonstrate the conversion reaction process in α-Fe_2O_3. The process was initiated through the reduction of Fe_2O_3 to Fe_3O_4 nanocrystals, which form 4-nm-nanoparticles within the nanowire. Further lithiation converted all of the iron oxides to BCC Fe nanocrystals with the significant growth up to 21 nm. During delithiation, the reactions proceeded in the reverse order, Fe^0-Fe^{2+}-Fe^{3+}. However, the initial single crystalline α-Fe_2O_3 nanowires were replaced by nanocrystalline ones after first cycle. The delithiated electrode maintains the nanowire geometry over many cycles due to the nature of the short-range cation diffusion that facilitates the process. Besides, nanowires covered with continuous carbon film exhibited much better electrochemical properties, such as cycle capacity, stability and conductivity, than the uncoated ones. The intrinsic conductivity improvement from α-Fe_2O_3 to Fe_3O_4 can further enhance the electrochemical performance.

ACKNOWLEDGEMENTS

It is a great opportunity to express my gratitude to ones contributing to my graduate education. Foremost, I would like to thank my advisor Prof. Shen J. Dillon for helping me go through all difficulties in my entire master studies. His intelligence and knowledge not only lead me to the fundamental science, but also inspire my interests in this area. His influences on me will last in the future.

I would like to thank all my group members, especially Kaiping Tai for his great experimental support and research discussion. Besides, I am deeply indebted to Ke Sun for his patient and professional peel review and bring my thesis to the current state. I would like to thank all the staffs in Materials Research Laboratory as well for their training and discussion on the characterization technics.

Finally, I owe my deepest gratitude to my family, especially my parents, aunt, uncle, cousin and girlfriend. My graduate study would not have been possible without their consistent support and encouragement.

TABLE OF CONTENTS

CHAPTER 1

INTRODUCTION

1.1 Fundamentals and Performance Matrix

Batteries store electrical energy in the form of chemical energy. Galvanic reactions spontaneously occur in an electrochemical cell when the circuit is connected by external electronic load if a certain mobile chemical species (like Li in lithium ion batteries) in the two electrode materials are at different chemical potential [1].

Lithium-ion batteries are one of the most commonly utilized secondary (rechargeable) batteries in portable applications. Lithium ion batteries are composed of four functional elements: a cathode, anode, electrolyte and separator. In the charge and discharge processes, oxidation/reduction reactions occur in the active materials in the two electrodes, accompanied by the lithium ions flowing through electrolyte and electrons flowing through external circuit (Figure 1.1) [2]. In this sense, the electrodes store and release energy through a redox reaction. The electrolyte facilitates lithium ion transport between electrodes and forces electrons to pass through the external circuit. The separator prevents direct contact between the electrodes, which would lead to shorting.

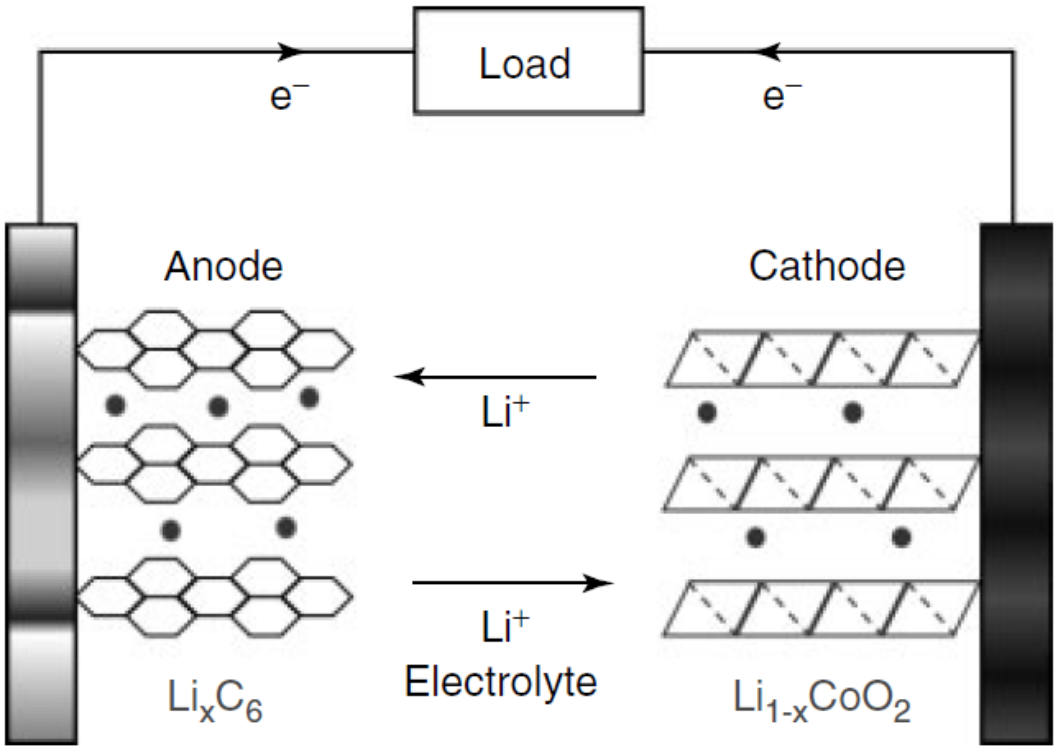

Figure 1.1 Illustration of the charge–discharge process involved in a lithium-ion cell consisting of graphite as the anode and layered $LiCoO_2$ as the cathode [2].

In order to better understand lithium-ion batteries, several definitions are introduced to characterize the properties (Table 1.1).

Table 1.1 Important Battery Characteristics [3]

Battery characteristics	**Definition**	**Unit**
Open - circuit voltage	The voltage in measured at zero current, often referred to as the value in the charged state.	Volt (V)
Current	The number of Coulombs passed per unit time	Ampere (A)

Table 1.1 (Cont.)

Battery characteristics	**Definition**	**Unit**
Specific energy density	The energy that can be derived per unit mass of the cell (or sometimes per unit mass of the active electrode material)	Watt - hours per kilogram (Wh/kg)
Power density	The power that can be derived normalized to a physical description of the sample (mass, volume, area)	Watt per kilogram (W/kg**)**
Capacity	The theoretical capacity of a battery is the number of Coulombs stored in the cell or electrode	Ampere - hours per gram (Ah/g)
Cycle life	The number of cycles completed before a 20% reduction in capacity	Cycles

1.2 Applications

The market for lithium ion battery has been continuously expanding, since the commercialization of first generation of lithium ion batteries in 1990s. So far they have penetrated every facet of our lives in applications ranging from consumer electronics and transportation to biomedical implants and space exploration

Batteries have received significant interest in recent years owing to their potential to electrify automotive transportation, which could result in more cleaner and more efficient utilization of energy. The energy efficiency of conventional internal combustion engines (ICE) typically falls below 25%, due to the thermal loss and idling. However, for battery-powered

vehicles, the energy efficiency can be several times higher than ICE, since the main loss is addressed to the resistance of the electric circuitry (Figure 1.2).

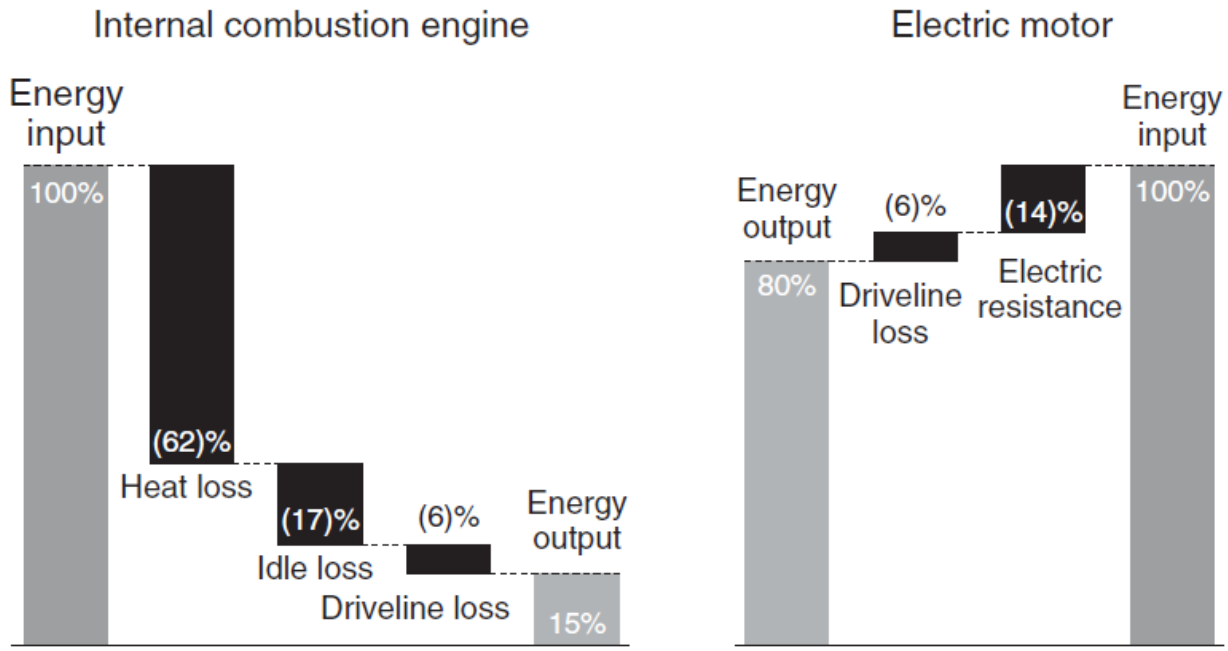

Figure 1.2 Comparison of an internal combustion engine with an electric motor on energy-to-wheels basis [4].

Another potential application for lithium-ion batteries is stationary energy storage. The current electricity generation is mostly based on fossil fuels, including coal, natural gas and oil. Demand for electrical power continues to expand, while fossil fuel reserves are depleting. Additionally, carbon-based combustion reaction products are believed by many to be driving climate change that could affect quality of life for humans. Therefore, the need for sustainable energy sources is urgent. Solar and wind are most abundant and accessible renewable energy sources. However, their intermittent nature does not correlate with demand and requires variable compensation from traditional power plants. In this sense, the development of large scale stationary energy storage system for load leveling and power conditioning is necessary. Table

1.2 provides performance and cost comparisons of potential grid scale battery technologies. Lithium ion batteries provide the highest efficiency, but also have the largest capital costs.

Table 1.2 Energy storage for utility transmission and distribution grid support [5].

Technology option	Maturity	Capacity (MWh)	Power (MW)	Duration (hours)	% Efficiency (total cycles)	Total cost ($/kW)	Cost ($/kWh)
CAES (aboveground)	Demo	250	50	5	(>10,000)	1950–2150	390–430
Advanced Pb-acid	Demo	3.2–48	1–12	3.2–4	75–90 (4500)	2000–4600	625–1150
Na/S	Commercial	7.2	1	7.2	75 (4500)	3200–4000	445–555
Zn/Br flow	Demo	5–50	1–10	5	60–65 (>10,000)	1670–2015	340–1350
V redox	Demo	4–40	1–10	4	65–70 (>10,000)	3000–3310	750–830
Fe/Cr flow	R&D	4	1	4	75 (>10000)	1200–1600	300–400
Zn/air	R&D	5.4	1	5.4	75 (4500)	1750–1900	325–350
Li-ion	Demo	4–24	1–10	2–4	90–94 (4500)	1800–4100	900–1700

1.3 Electrode Materials and Relevant Reaction Mechanisms

Due to the reaction mechanisms associated with Li, the electrode materials can be classified into three categories, intercalation hosts, alloying/dealloying reactions, and conversion reactions (Figure 1.3).

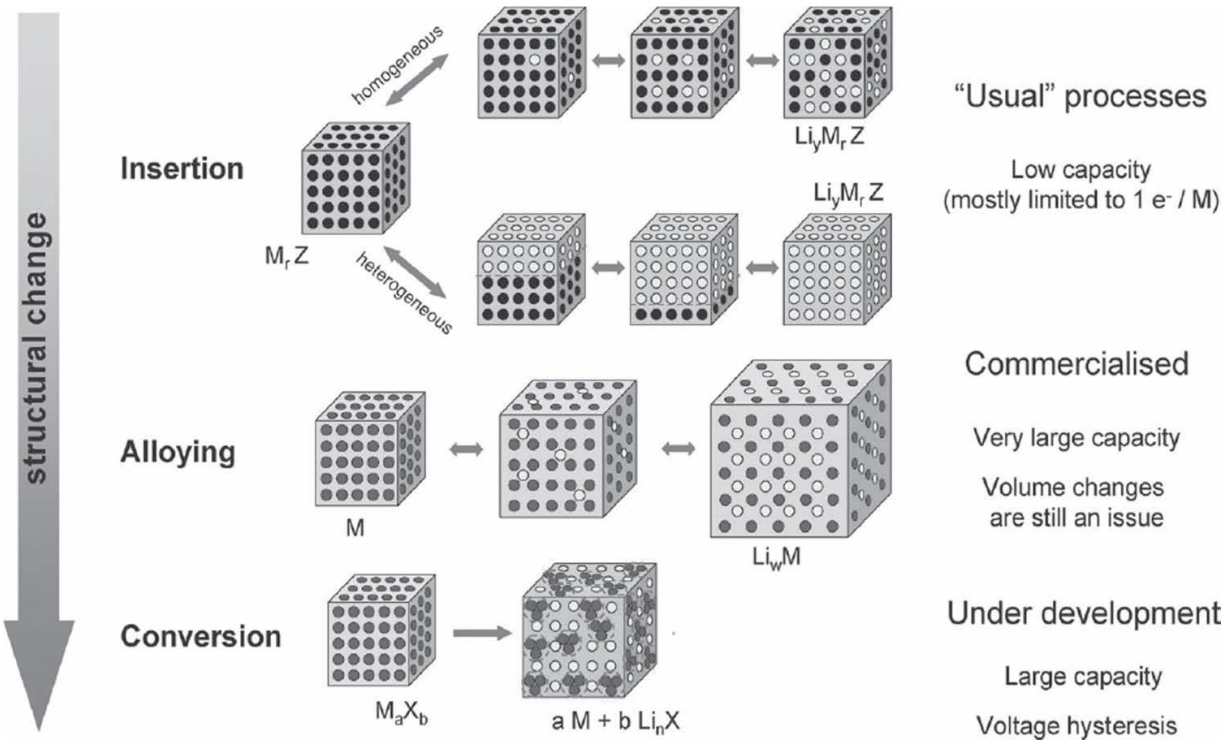

Figure 1.3 Schematic illustration of the reaction mechanisms of electrode materials with Li ions in LIB [6].

$LiCoO_2$ intercalation cathodes and carbon-based intercalation anodes have historically been the commercial electrodes of choice [7]. However, other systems based on $LiFePO_4$, $LiMn_2O_4$ and $Li_4Ti_5O_{12}$ have also found commercial application recently. These systems exhibit decent cycle life due to the relative stability of the crystal structure during intercalation and deintercalation when performed in a chemical window where irreversible reactions do not occur. However, this is also the handicap to achieve high capacity, since the crystal structure only maintains stability within a narrow range of Li content [8]. A variety of other systems have also been considered at the laboratory scale.

Alloying electrodes have been studied as high capacity Li hosts. Metals and semimetals, which alloy with lithium at room temperature, usually achieve much higher capacity than the

intercalation electrodes (3590 mAh/g for Si and 991 mAh/g for Sn). However, the drastic volume change associated with the reaction results in large strain gradients in the particles. The fracture of these particles may lead to failure either directly, through loss of electronic percolation, or indirectly, through associated interfacial and side reactions. Also, the rate capability of these electrodes is limited due to solid-state diffusion and the high capacity. A variety of approaches have been demonstrated to improve their performance, primarily through nanostructuring [9], but few are commercially viable. Unfortunately, alloying electrodes are not appropriate as cathode materials since Li is present in a reduced state, which limits the equilibrium voltage associated with the reaction. Increasing the capacity of the anode does not significantly improve the capacity of the entire battery without significant increases in cathode capacity.

In 2000, a third Li electrode reaction, namely the conversion reaction, was introduced [10]. This category mainly comprises transition-metal oxides (MX, where M is Fe, Ni, Co, Cu, etc. and X=O, F, Cl, etc.). Generally, this group of materials can achieve relatively high capacity without drastic volume change. Unlike alloying and intercalation reactions, lithiation involves reduction of the host. This typically results in transition-metal nanoparticles (1~5 nm) precipitating, in a matrix of amorphous lithium oxide. The transition-metal nanoparticles re-oxidized during delithiation. The overall reaction is expressed in Equation 1.1. This reaction tends to occur in systems where the transition metal is in a low oxidation state and is not amenable to reduction to a lower oxide and systems where the crystal structure does not accommodate Li.

$$2Li^+ + MO + 2e^- \leftrightarrow Li_2O + M \text{ (M = Fe, Ni, Co, Cu, etc.)} \quad (1.1)$$

In order to investigate the evolution of crystallinity of conversion reactions upon cycling, CoO was investigated by in-situ X-ray diffraction (XRD) by P. Poizot [10]. As lithiation proceeded, a continuous decrease in CoO Bragg reflections occurred. Two electrons per Co atom were consumed during reduction reaction. However, metallic Co was not detectable in the diffraction pattern because the nanoparticles were presumably smaller than the X-ray coherence length (Figure 1.4).

Conversion reaction based Li hosts have great potential because they might function as both anodes and cathodes that have high capacity [6]. They can also achieve reasonable cycle life and may be produced from abundant low cost precursors. Unfortunately, many of these systems exhibit large hysteresis that makes them too inefficient for commercial application [6]. This thesis seeks to investigate the fundamental mechanisms associated with Li-based conversion reactions in model host systems based on iron oxides. Improved insights into the reaction process should help drive new approaches to limiting hysteresis and demonstrating commercially viable conversion reaction electrodes.

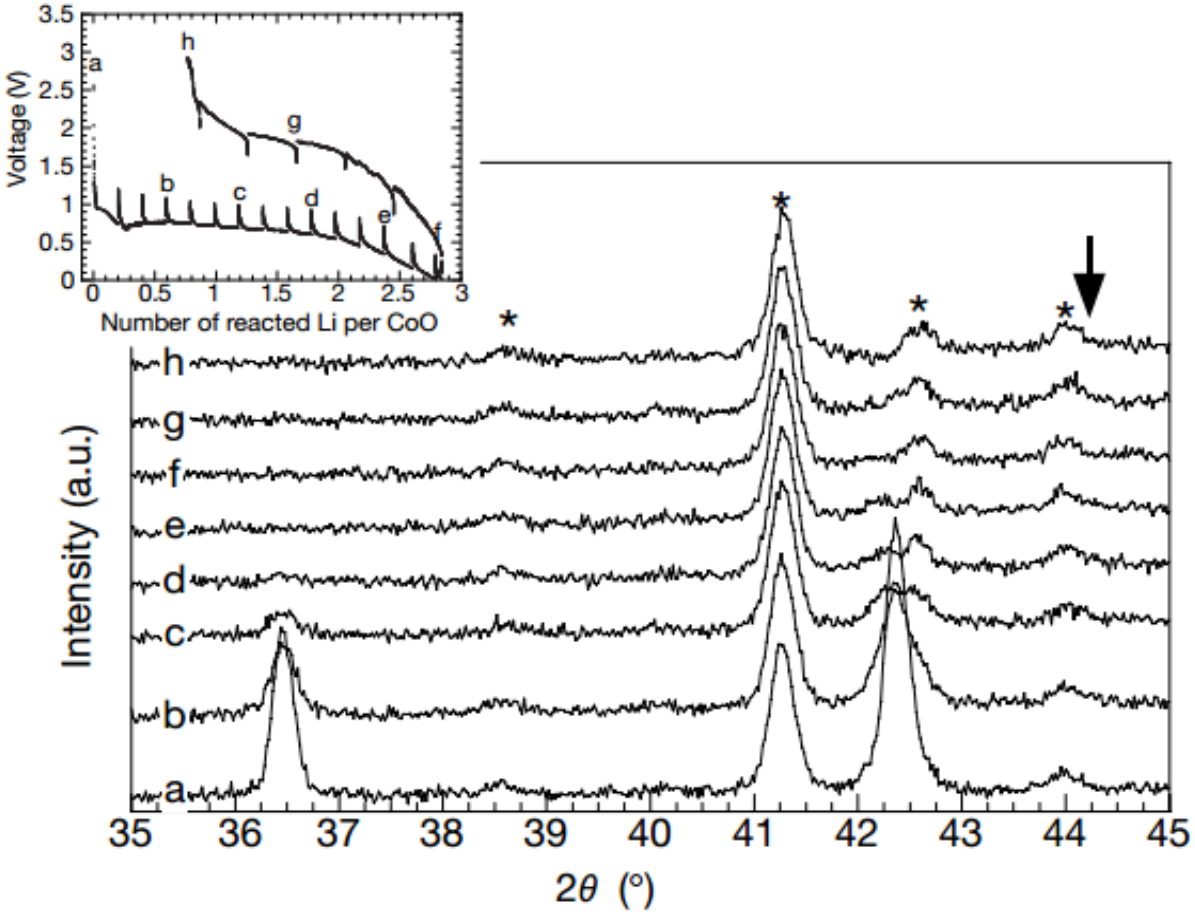

Figure 1.4 In-situ X-ray diffraction patterns collected at various states of discharge and charge of a CoO/Li electrochemical cell. Inset, the voltage-composition profile for such a cell, where the letters a to h denote the x values (in Li_xMO) at which the corresponding X-ray patterns were taken. Such an experiment was performed in a galvanostatic intermittent mode, using current-on periods of two hours at a rate of C/10, separated by two-hour open-circuit periods during which X-ray data were taken. The peaks marked with an asterisk correspond to Be and BeO, and the arrow indicates where a Bragg peak corresponding to metallic Co should appear [10].

CHAPTER 2

STRUCTURAL EVOLUTION OF α-Fe_2O_3 NANOWIRES DURING LITHIATION/DELITHIATION

2.1 Background and Research Goal

Various schemes for realizing high capacity electrode materials for lithium ion batteries have been proposed and investigated in the past two decades to meet growing demand for portable and mobile energy storage [11-15]. Electrodes may accommodate lithium through intercalation, alloying, or conversion reactions. Intercalation electrodes typically exhibit relatively low capacities, due to constraints imposed by crystal structure and valence changes. Alloying electrodes possess large capacities, but typically exhibit large strains and associated degradation processes that limit their cycle life [16,17]. The voltage window of alloying electrodes prohibit their use as practical cathodes and therefore only provide limited improvement to overall energy density of cells containing low capacity cathodes. Conversion reaction electrodes have large capacities and could function as either anodes or cathodes, depending on their chemistry. However, they exhibit significant hysteresis that limits their efficiency and may be reasonably susceptible to capacity fade. If novel nanostructuring approaches could be realized to improve the reversibility and reduce the hysteresis associated with conversion reactions, significant improvements in the energy density of lithium ion batteries might be realized. Here we seek to characterize the nanostructural evolution of a model conversion reaction electrode, α-Fe_2O_3, in order to gain improved insights into the mechanisms associated with the process.

Fe_2O_3 has been widely studied due to its abundance, low cost, and interesting magnetic, semiconducting, and electrochemical properties [13-35]. According to in-situ x-ray diffraction studies performed by Larcher et al. [18,23], 20 nm Fe_2O_3 particles first accommodate lithium ions by forming a hexagonal $LiFe_2O_3$ phase. A phase transformation from a phase with a close-packed hexagonal anion lattice (α-$LiFe_2O_3$) to a disordered cubic structure ($Li_2Fe_2O_3$) occurs upon further lithiation. Iron nanoparticles (< 2 nm determined from X-ray peak broadening) precipitate in an amorphous Li_2O matrix, which forms simultaneously during deep discharging. Equations (2.1) - (2.3) described the process proposed based on X-ray analysis [23]:

$$\alpha\text{-}Fe_2O_3 + Li^+ + e^- \rightarrow \alpha\text{-}LiFe_2O_3 \quad (1)$$

$$\alpha\text{-}LiFe_2O_3 \rightarrow \text{cubic } Li_2Fe_2O_3 \quad (2)$$

$$\text{cubic } Li_2Fe_2O_3 + Li^+ + e^- \rightarrow Fe^0 + Li_2O \quad (3)$$

The characteristic microstructural length scales associated with the process are deemed critical to the function of these electrodes. Particle size measurements based on X-ray diffraction may be strongly affected by others factors (e.g. strain, defects, or contamination), which motivate the need for a direct measurement. In this paper, we report a simple approach to growing α-Fe_2O_3 single crystal nanowires and characterization of the lithiation and delithiation process, sampled at different states of charge, in a binder and carbon free system, by transmission electron microscopy (TEM).

2.2 Experiments and Characterization

Single crystal α-Fe_2O_3 nanowires were synthesized by Joule heating of ~220 μm diameter iron wire (99.99%, Goodfellow) under ambient conditions [36]. The iron wire was cut to ~10 cm long pieces, cleaned in dilute hydrochloric acid (2% in volume) for several minutes, and rinsed by acetone, alcohol, and deionized water. AC power (~4 W at 60 Hz) was applied to the ends of the wire to induce oxidation for ~10 mins (Figure 2.1). This produces a high density of high aspect ratio α-Fe_2O_3 nanowires.

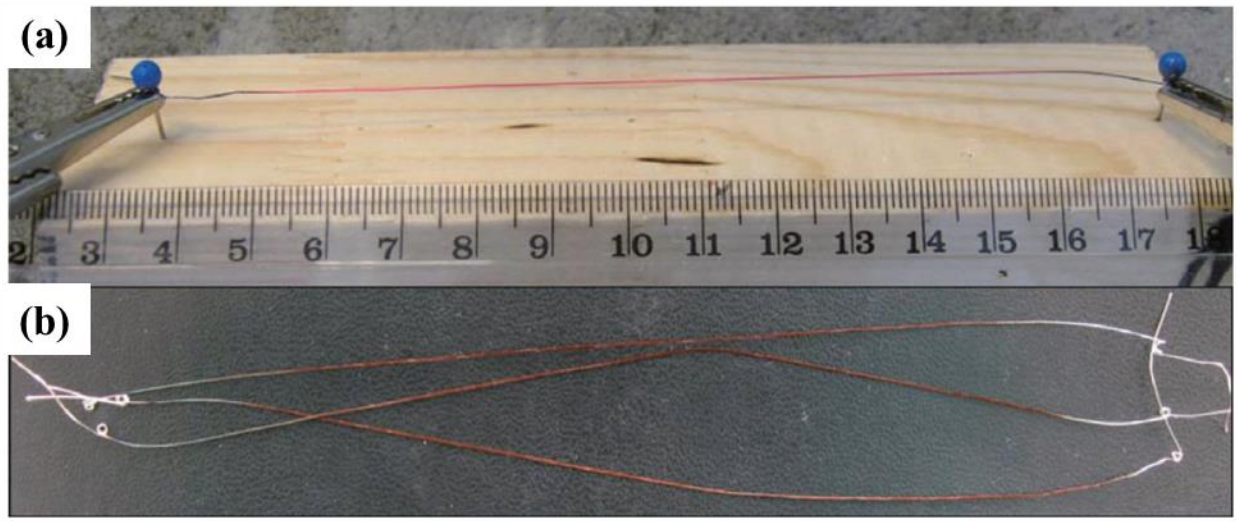

Figure 2.1 Pictures demonstrating simplicity of the proposed method: (a) the process of nanowire growth; (b) iron wires after resistive heating treatment [36].

The electrochemical properties of the α-Fe_2O_3 nanowires were characterized in a glass vial cell within a dry Ar-filled glovebox (Mbraun Labstar) (Figure 2.2). The iron wire served as the current collector for the α-Fe_2O_3 nanowires on the surface. This was cycled against a metallic lithium counter electrode in ethylene carbonate (EC) dimethyl carbonate (DMC) (1:1 by volume) 1 M $LiPF_6$ electrolyte. The electrochemical tests were carried out using a computer-controlled

potentiostat/galvanostat (SP200, Biologic Co.). Samples were cycled to different states of charge (0.9 V, 0.8 V, 0.7 V, 0.6 V and 0.5 V) by slow scan cyclic voltammetry (CV) performed at 50 μV/s. The slow scan rate was selected to allow the nanowires to approach equilibrium during cycling, without having to fully lithiate the dense underlying oxide. To investigate the fully lithiated and delithiated states, the samples were also maintained at a constant potential of 0.1 V and 2.0 V for 3 h, respectively, after the potential sweeps. All of the tested samples were washed by propylene carbonate (PC) and acetone, and then dried in the glove box.

The microstructures of the α-Fe_2O_3 nanowires were characterized by scanning electron microscopy (JEOL-6060LV), transmission electron microscopy (JEOL-2010Lab_6 and JEOL-2010Cryo), and electron energy loss spectroscopy (EELS) in the scanning transmission electron microscopy (JEOL-2010F EF-FEG).

The mean diameter of α-Fe_2O_3 nanowires were averaged based on measurements taken at the middle of each nanowire. All the nanocrystals in dark-field (DF) images were assumed to be approximately spherical and their diameters were calculated in terms of areas (S) measured from each particle ($D = 2 * \sqrt{S/\pi}$).

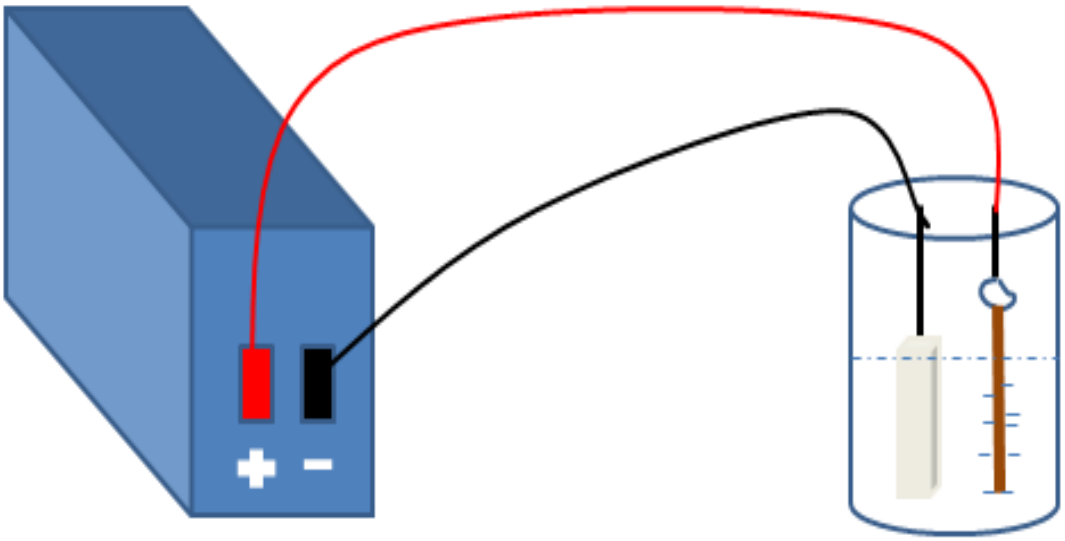

Figure 2.2 Battery setup is prepared by connection between Potentiostat Analyzer (left) and glass vial (right) including metallic lithium as anode, Fe wire with Fe_2O_3 nanowire as cathode and electrolyte.

2.3 Results and Discussion

2.3.1 Single Crystal α-Fe_2O_3 Nanowire Characterization

Nanowires, several microns in length (Figure 2.3a-e) with an average diameter of ~105 nm, emerge from an underlying dense oxide shell. The corresponding selected area electron diffraction (SAED) pattern (Figure 2.3f) indicates that the Fe_2O_3 nanowire growth occurs along [110] axis [36], which is also confirmed by the d-spacing imaged by high-resolution TEM (Figure 2.3g).

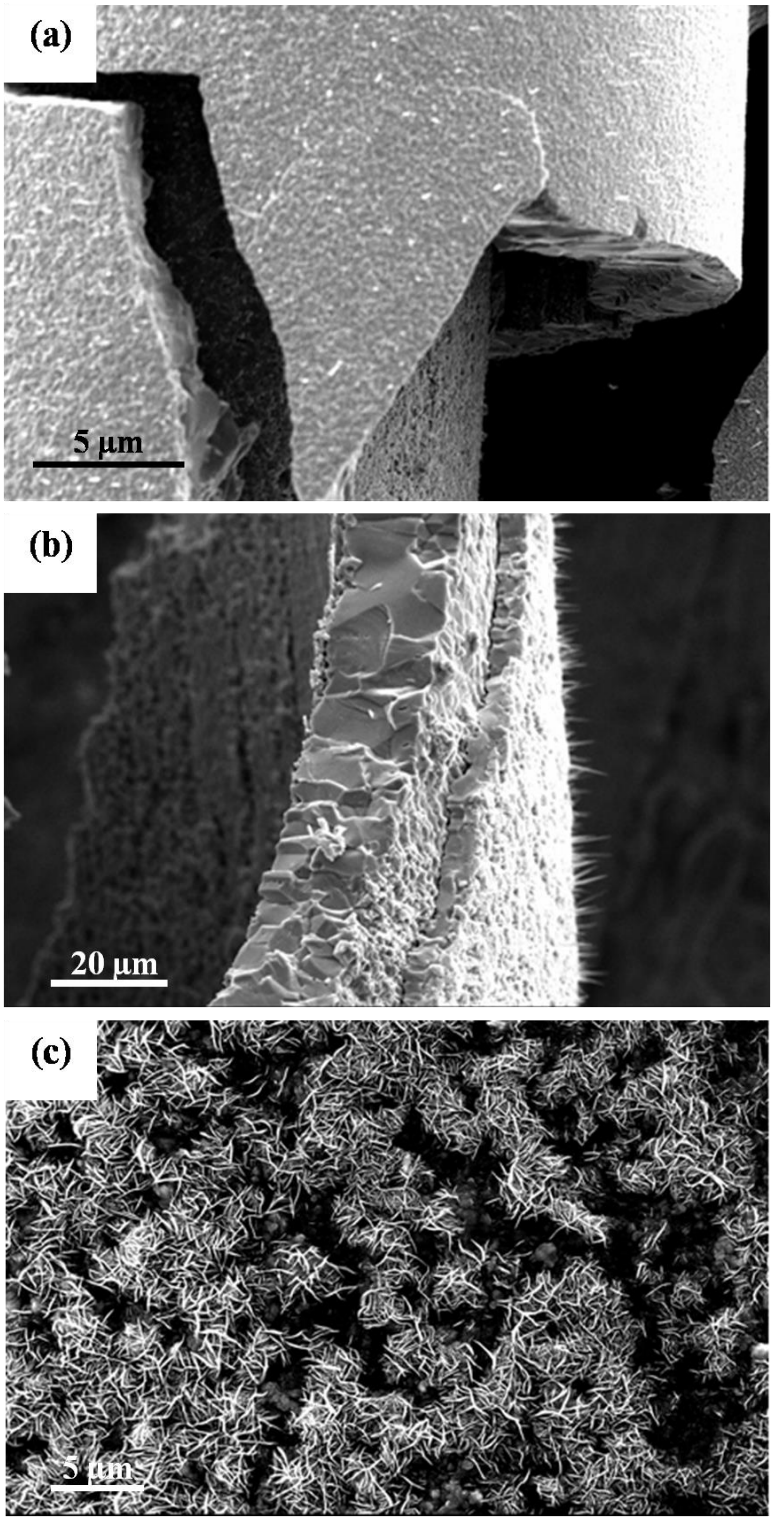

Figure 2.3 (Cont.)

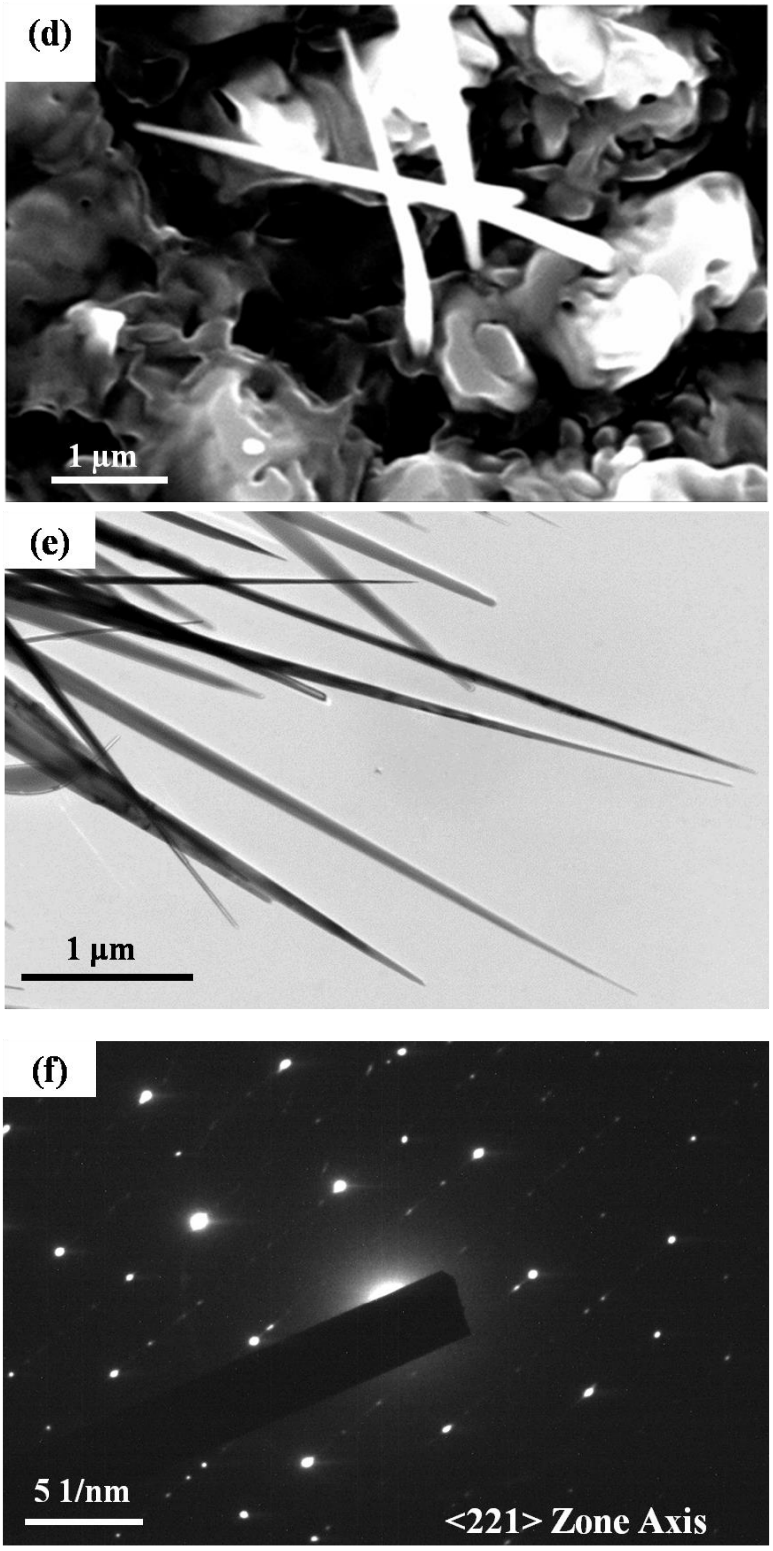

Figure 2.3 (Cont.)

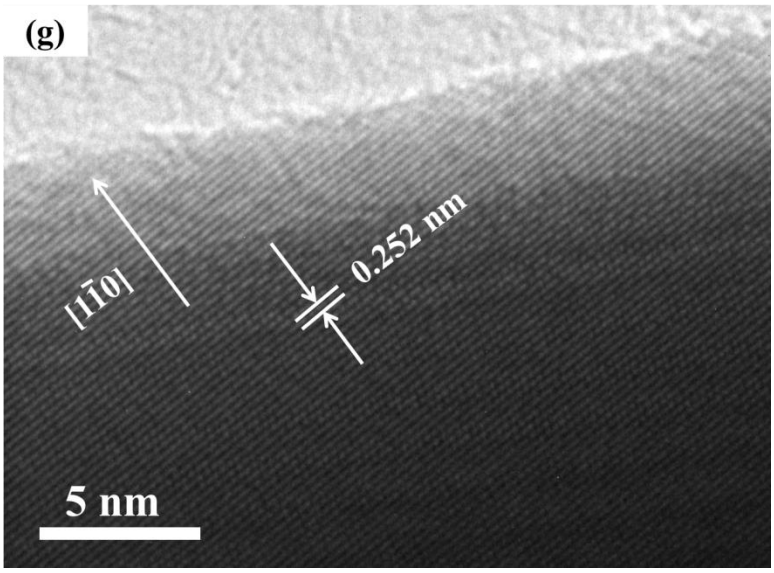

Figure 2.3 SEM images of prepared Fe_2O_3 nanowire on the core-shell structure (a-d), TEM images, SAD pattern of Fe_2O_3 nanowire and high-resolution image (e-g).

2.3.2 Electrochemical Properties

Figure 2.4 depicts a cyclic voltammogram acquired at a sweep rate of 500 μV/s in the range of 0.25~2.5 V. A small pre-peak and shoulder peak emerge near 0.9 V and a primary lithiation peak occurs near 0.7 V. A single delithiation peak appears near 1.7 V. All of the peaks are reasonably broad. Similar peaks were observed in subsequent cycles, with some changes in the intensity.

Reddy et al. [19] have reported CV results for α-Fe_2O_3 nanoflakes up to 15 cycles at a sweep rate of 58 μV/s, in which the reduction and oxidation peak appear at 1.0 and 2.0 V, respectively. Chen et al. [20] published the results of 20 CV cycles performed at 500 μV/s where the reduction and oxidation peaks occur at 0.5 and 2.1 V, respectively. Our current results fall within a similar range. Differences in peak positions may be accounted for by generic differences

in the overall polarization of the cell. Interestingly, in the present study, the anode consists of ~10 μm Fe_2O_3 nanowires without any additional conductive agents but display relatively low polarization.

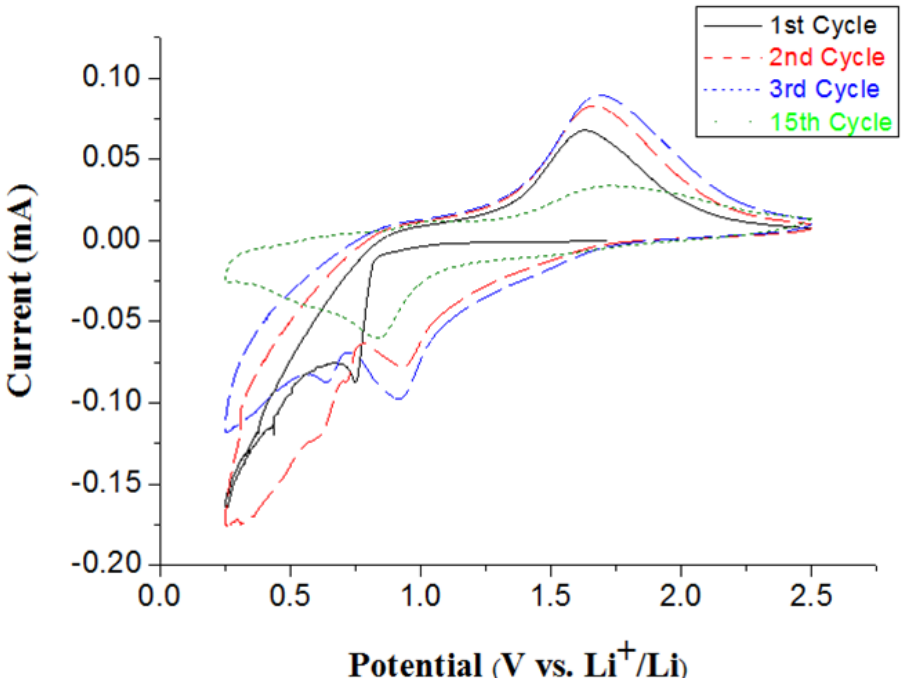

Figure 2.4 Cyclic voltammetry of α-Fe_2O_3 nanowire with scan rate of 500 μV/s at 20 °C.

2.3.3 Ex-situ TEM Investigation

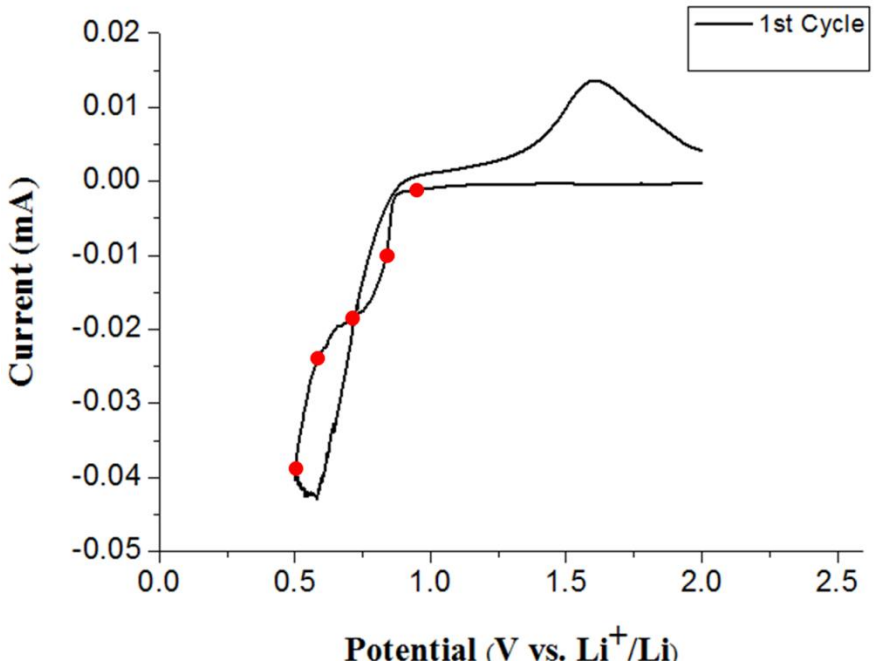

Figure 2.5 Cyclic voltammetry of α-Fe_2O_3 nanowire with scan rate of 50 μV/s at 20 °C.

Figure 2.6a-l shows the TEM micrographs and SAED patterns from Fe_2O_3 nanowires at various stages of lithiation (Figure 2.5). Beginning at 0.9 V, a thin surficial layer forms that relates to solid electrolyte interphase (SEI) formation. The SAED pattern still exhibits prominent single crystal diffraction spots with very weak diffraction rings, indicating limited conversion reaction has occurred at this point. At 0.8 V, bright-field TEM imaging revealts a moderate density of dark spots distributed about the nanowires, which were confirmed by the dark field TEM to be ~4.3±0.3 nm nanocrystals. Corresponding SAED rings can be indexed to Fe_3O_4. After further cycling to 0.7 V, an increased density of nanocrystals emerges throughout the nanowire, with little change in their average size of 4.1±0.4 nm. These spots are still indexed as Fe_3O_4, as shown in the Figure 2.6i. After lithiation to 0.6 V, the average size of the nanocrystals decreases to 2.9±0.2 nm. At this stage, BCC Fe exists as the only phase in the diffraction pattern.

After lithiation to 0.5 V, a thick SEI layer forms and the average diameter of the nanowires increases encase the nanowires. The dark field imaging reveals a uniform dispersion of nanocrystals throughout the nanowire and their size sharply increases to 21±1.7 nm.

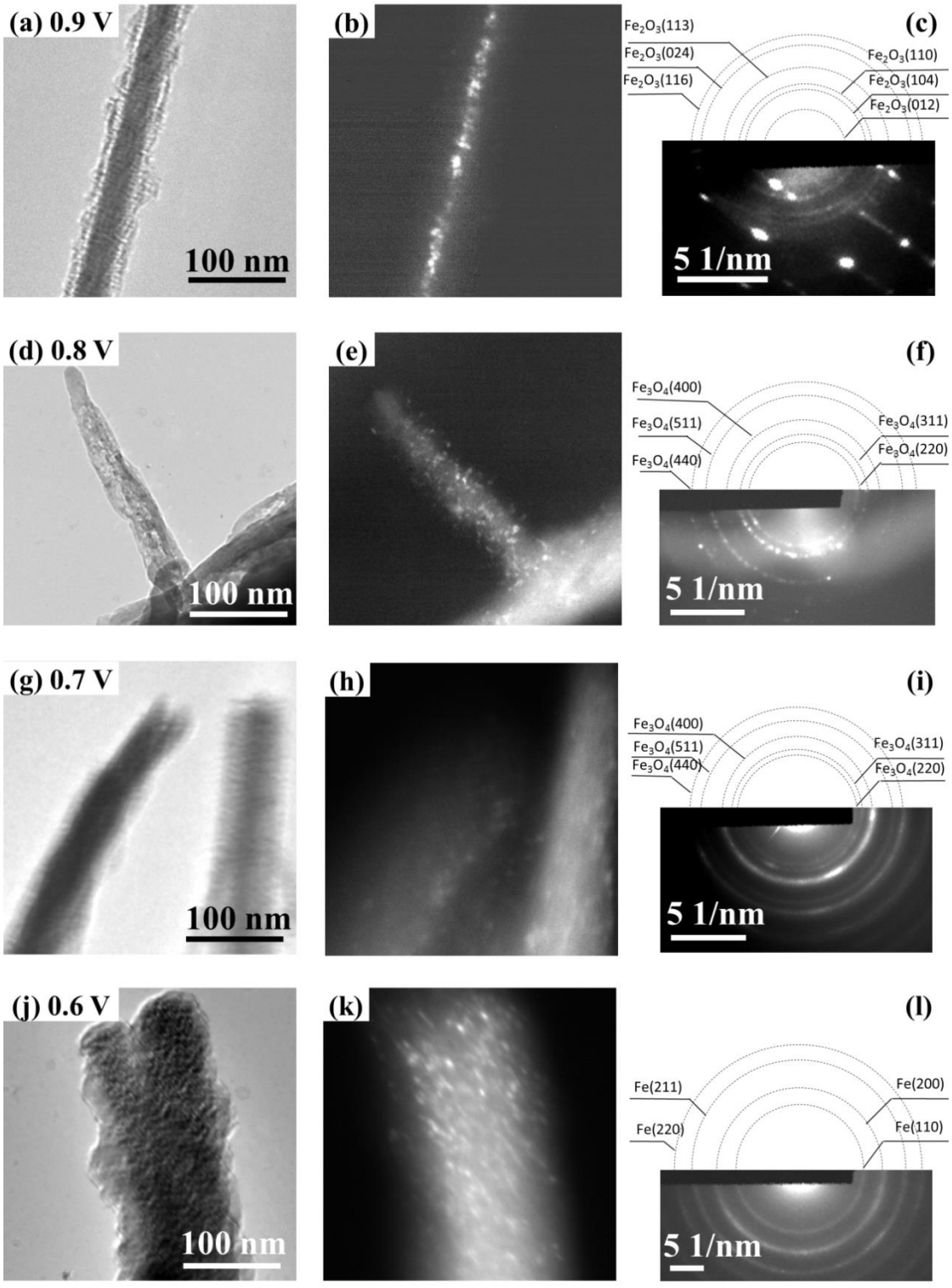

Figure 2.6 (left) Bright field TEM images, (middle) dark field TEM images, and (right) SAED patterns of α-Fe_2O_3 nanowire discharged to 0.9, 0.8, 0.7 and 0.6 V.

To investigate the situaton of reversed reaction, the samples are subsequently delithiated by cycling to 2 V and holding for 3 h. As shown in Figure 2.7, the nanocrystalline Fe is reoxidized, producing nanocrystalline Fe_2O_3 with an average size of 7.7±0.8 nm.

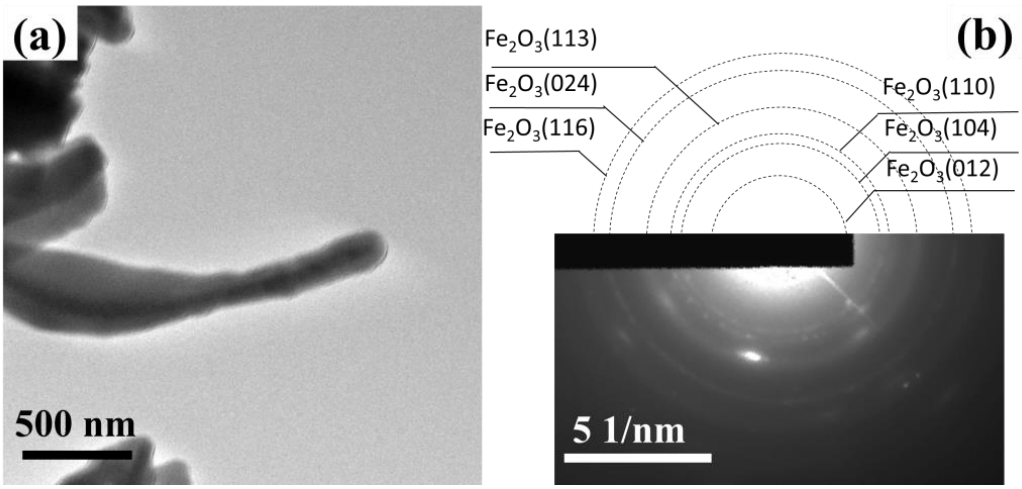

Figure 2.7 Bright field TEM image (a) and SAD pattern (b) of α-Fe2O3 nanowire charged at 2 V for 3h.

Nanowires after 30 cycles of charge-discharge were also characterized (Figure 2.8). Since the SEI is as thick as several micrometers, we simply cleaned the SEI by e-beam, in order to observe the essential nanowire. The SEI, containing certain kinds of organic lithium salts, decomposes when irradiated by high energy electrons. The interesting thing is that although the surface becomes rougher than original one, the nanowire frame still survived even after 30 cycles, indicating decent reversibility and stability.

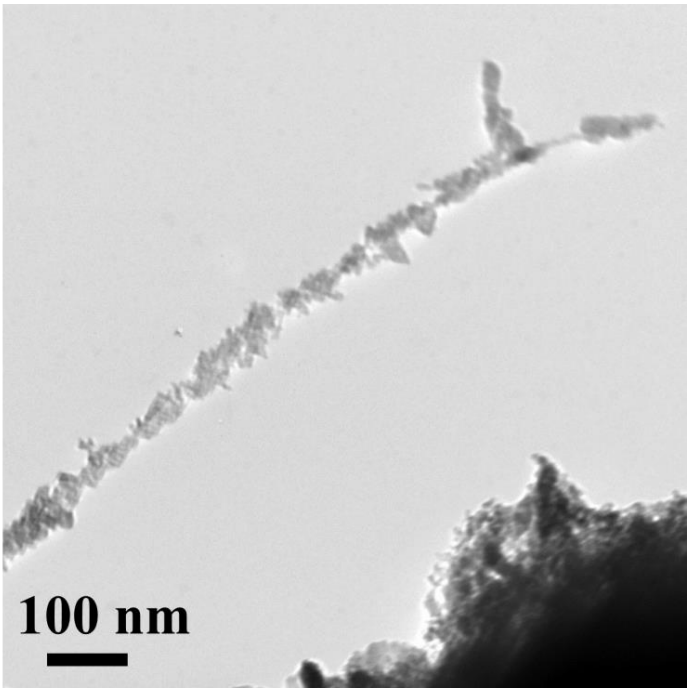

Figure 2.8 Bright field TEM image of Fe_2O_3 nanowire after 30 cycles.

A sample held at constant potential of 0.1 V for 3 h was subsequently characterized by STEM. The element distribution across the lithiated nanowire was analyzed by EELS as shown shown in Figure 2.9. Carbon detected across the entire nanowire relates to the organic components of the SEI. The signal from lithium is relatively uniform across the nanowire. Although signals from iron and oxygen cannot be collected in the core area due to the increasing thickness, which affects the signal to noise ratio, the tendency can be seen that the Fe/O intensities are gradually enriched from the edge to the core of the nanowire. Smilarly, the Z-contrast STEM image suggests that the nanowire, after complete lithiation, has a core/shell structure. The shell part primarily consists of light elements, which include Li/O/C from the SEI. The core contains O, Li, Fe, and C, but some of the light element contribution may result from the projection of the shell region. These results indicate that lithium ions diffuse into the Fe_2O_3 nanowire, while Fe and O, which have much lower diffusivities, remain within the initial

nanowire boundaries. This could also explain the persistence of the nanowire over multiple cycles without geometric changes.

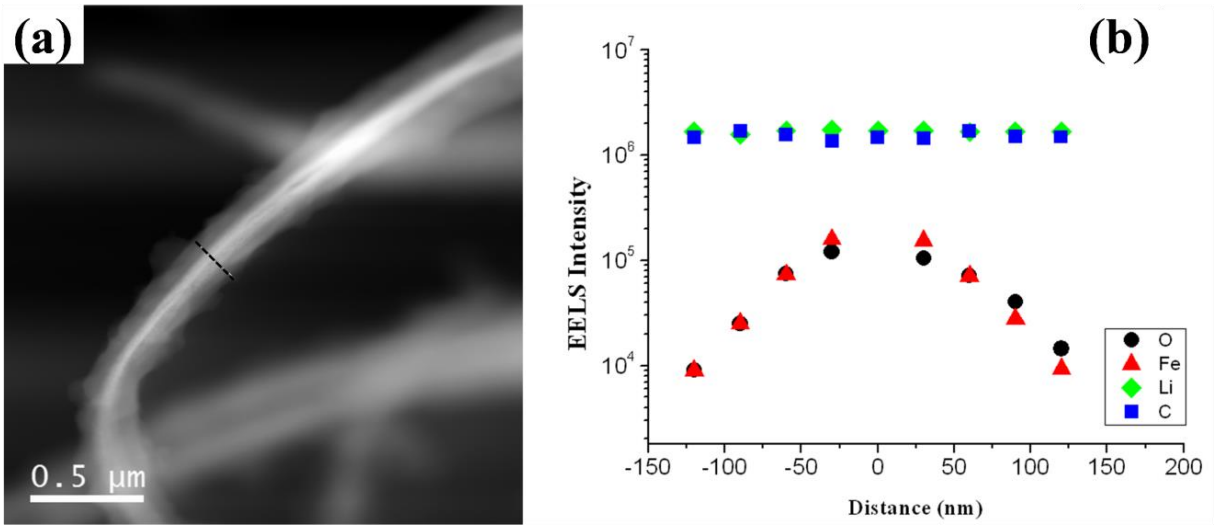

Figure 2.9 Integrated peak counts from EELS as a function of distance across a lithiated nanowire. Data taken from region indicated in image.

The Fe_3O_4 nanocrystals precipitate with average size of 4.3 nm. Their size does not increase with further reaction, but instead their number density increases. The phenomenon likely results from limits on continued reaction due to solid-state diffusivity and a lack of coarsening that is also limited by diffusion. The appearance of Fe nanocrystals at 0.6 V accompanies a ~30% reduction in nanoparticle size to 2.9 nm. The loss of oxygen from individual Fe_3O_4 particles can account for this size reduction. Our measurement of nanocrystal size is reasonably consistent with the simulation of the FeF_3 system (2~3 nm). After cycling to 0.5 V, a pronounced increase in grain size to 21 nm occurs. The two-phase microstructure likely limits coarsening and grain growth. The Fe particle size likely increases due to propagation of the reaction fronts. After charging to 2.0 V, the particle size decreases again to 7.7 nm. During lithiation and conversion of Fe_xO to Fe^0, diffusion of $Fe^{2+/3+}$ out of Fe_xO likely limits the reaction,

while $Fe^{2+/3+}$ diffusion into Li_2O likely limits the delithiation process. The difference in characteristic particle sizes results from the difference in the Fe cation diffusivities in these two oxides.

α-Fe_2O_3 electrically insulates well at room temperature (electron conductivity $\sigma \sim 10^{-8}$ S/m). Charge transport across ~10 μm of this material is significant. However, the polarization in CV is smaller than that reported for nanoparticles in conventional coin cells with conductive agents present. Surface transport may facilitate the initial reaction which results in the formation of the Fe_3O_4, which displays significantly higher electron conductivity ($\sigma \sim 10^{-2}$ S/m). An increase in the amount of charged defects and interfaces during the first cycle could account for the reduction in polarization observed in the first few cycles.

The overall results for the phase evolution during lithiation and delithiation of α-Fe_2O_3 nanowires characterized by TEM differ from those obtained for nanoparticles characterized by XRD. The reaction sequence determined here follows;

$$3\ \alpha\text{-}Fe_2O_3 + 2\ Li^+ + 2\ e^- \rightarrow Li_2O + 2\ Fe_3O_4 \qquad (3.4)$$

$$Fe_3O_4 + 8\ Li^+ + 8\ e^- \rightarrow 4\ Li_2O + 3\ Fe \qquad (3.5)$$

The source of the difference is unclear, but it may relate to the difference in sample geometry. The larger nanowires may not be able to accommodate a strained lattice necessary to support α-$LiFe_2O_3$. This may alter the subsequent phase evolution as the nanowires initially form Fe_3O_4 nanoparticles as a result of the conversion reaction. The system investigated by Larcher et al. initially refined its crystallite size through the formation of $Li_2Fe_2O_3$. $Li_2Fe_2O_3$ and

Fe_3O_4 are clearly differentiated by diffraction, thus the evolution of these two systems is believed to be distinct. In the final stage, both systems result in Fe nanocystals and Li_2O.

2.4 Conclusion

Lithiation of single crystal Fe_2O_3 nanowires proceeds by the initial reduction to Fe_3O_4 nanoparticles, and subsequent reduction to BCC Fe^0. Both processes produce Fe-based reaction products in the form of nanocrystals and Li_2O. During delithiation the Fe^0 reverts to Fe_2O_3. The delithiated electrode maintains the nanowire geometry over many cycles due to the nature of the short-range cation diffusion that facilitates the process.

CHAPTER 3

OPTIMIZATION OF Fe_xO_y AS ANODE FOR LI-ION BATTERIES

3.1 Introduction and Background

Accumulated study on Li ion batteries in the past two decades ensures its maturity to intrude the large scale energy storage market. Li ion battery is realized as one of the most promising complementary and high-round-efficient devices for the intermittent renewable energy system. Rather than that, hybrid and electric vehicles, driven by electrochemical energy from Li ion battery, are expected to be prevailing within the next 50 years.

Fe_xO_y is realized as the one of the most promising conversion reaction materials as anode for Li-ion batteries, due to the high capacity (1007 mAh/g for Fe_2O_3 and 900 mAh/g for Fe_3O_4 [37,38], abundance, bio-compatibility and low cost. Nevertheless, the poor electronic conductivity and size effect are believed to be the dominant handicaps for Fe_xO_y in the essentially commercial application. Therefore, various nano-structural materials are designed and synthesized with carbonous coating [37-47]. To further improve the electronic conductivity of the electrode, nano-strucures directly grown on the current collector are favored due to the much less contact resistance associated with chemical bonding between active materials and substrates [48].

Here, we first prepared the α-Fe_2O_3, α-Fe_2O_3 with carbon coating (α-Fe_2O_3-C) and Fe_3O_4 with carbon coating (Fe_3O_4-C) single crystal nanowires directly grown on the current collector. We seek to investigate their electrochemical properties for Li ion battery and filter the best one among this category.

3.2 Experiments and Characterization

Preparation of α-Fe_2O_3 single crystal nanowires: ~220-μm diameter iron wire (99.99%, Goodfellow), ~10-cm long, was cleaned in dilute hydrochloric acid (2% in volume) for several minutes, and rinsed by acetone, alcohol, and deionized water. Then it was applied to AC power (~4 W at 60 Hz) for ~10 mins to oxide under ambient conditions by Joule heating method [36].

Preparation of α-Fe_2O_3-Csingle crystal nanowires: The resulting α-Fe_2O_3 single crystal nanowires were carbon coated in the furnace at 500℃ for 5 h. Toluene vapor was blown into furnace with Ar, serving as carbon source.

Preparation of Fe_3O_4-C single crystal nanowires: ~220-μm diameter iron wire (99.99%, Goodfellow) was first cleaned in the same way of the α-Fe_2O_3 preparation. Then it was pre-oxided by being heated to 250℃ on the hotplate in air for 0.5 h. Further heat treatment was processed in the furnace at 500℃ with pure copper foil wrapped, in Ar and toluene atmosphere.

Electrochemical property evaluation: The prepared nanowires were tested in a vial cell within a dry Ar-filled glovebox (Mbraun Labstar). The iron wire served as the current collector for the nanowires on the surface. This was cycled against a metallic lithium counter electrode in ethylene carbonate (EC) dimethyl carbonate (DMC) (1:1 by volume) 1 M $LiClO_4$. The electrochemical tests were carried out using a computer-controlled potentiostat/galvanostat (SP200, Biologic Co.). Cyclic voltammetry (CV) was scanned at 500 μV/s. The rate performance of Fe_3O_4 nanowires were carried out at various current densities (0.2 mAh/cm^2, 0.4 mAh/cm^2, 0.8 mAh/cm^2 and 1.6 mAh/cm^2).

Charaterization: The pristine and reacted nanowires were investigated by scanning electron microscopy (JEOL-6060LV) and transmission electron microscopy (JEOL-2010Lab_6 and JEOL-2010Cryo).

3.3 Results and Discussion

Figure 3.1 represents the scanning and transmission electron microscope images of the pristine α-Fe_2O_3, α-Fe_2O_3-C and Fe_3O_4-C single crystal nanowires prepared. Large amount of nanowires were directly grown on the iron wire with various length (2~10 μm for Fe_2O_3 and 5~20 μm for Fe_3O_4). The bush-like Fe_3O_4 nanowires exhibit striking density compared to the other two. α-Fe_2O_3, α-Fe_2O_3-C nanowires are in the needle shape with decreasing diameter, while Fe_3O_4-C nanowires are more uniform in diameter. Copper nano-particle (Figure 3.1h), on the top of the Fe_3O_4 nanowire, behaves as the catalyst during the synthesis. According to each of the selected area electron diffraction (SAED) pattern (Figure 3.1c, f and i), the prepared nanowires are in the form of single crystal with little defects.

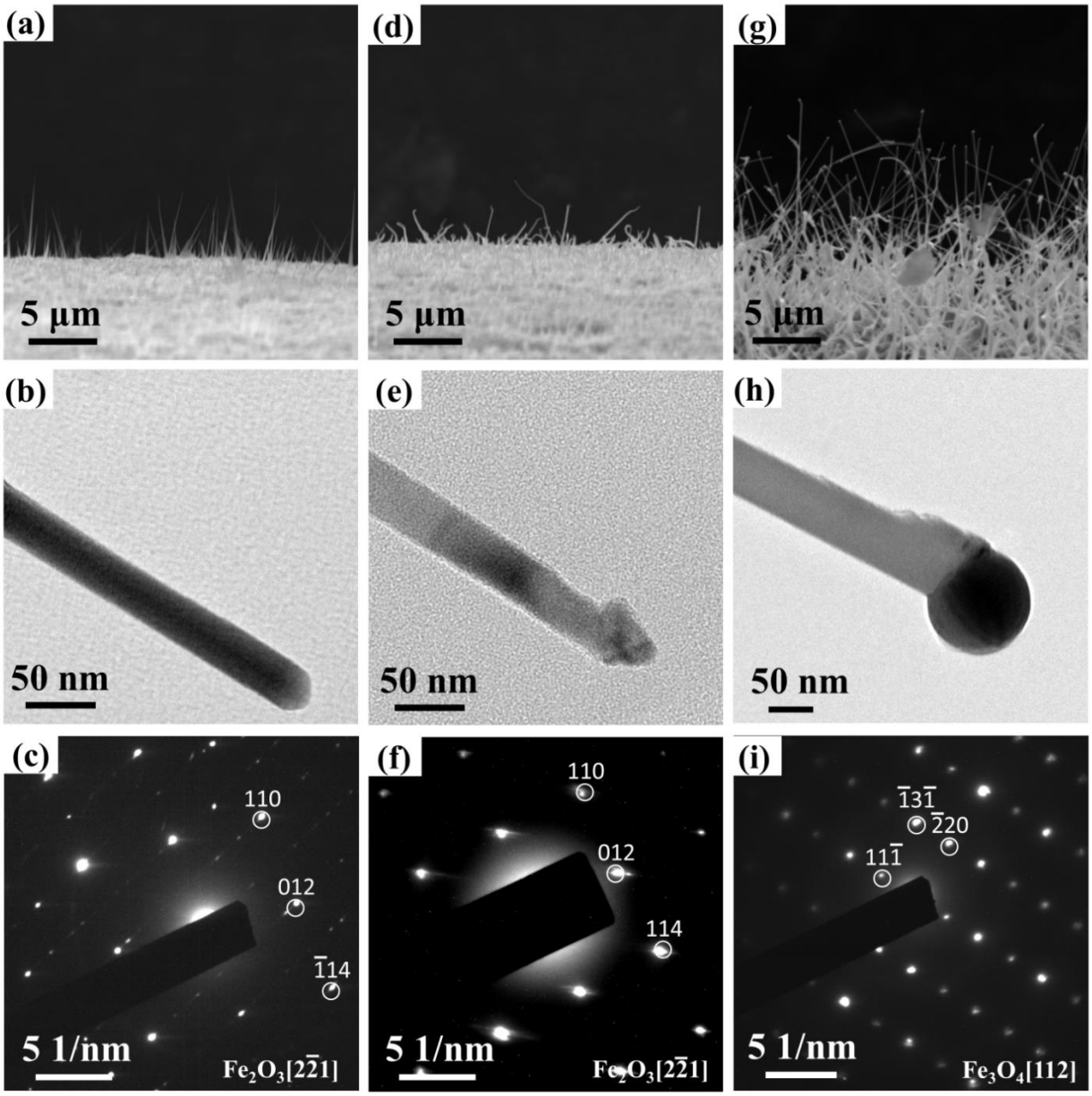

Figure 3.1 SEM, TEM image and selected area electron diffraction (SAED) pattern of prepared nanowires: α-Fe_2O_3 (a~c), α-Fe_2O_3-C (d~e) and Fe_3O_4-C (g~i).

Figure 3.2 shows the cyclic voltammetry of three kinds of nanowires with scanned rate of 500 μV/s in the range of 0.25~2.5 V vs. Li^+/Li. The first anodic peak of all the samples starts at 0.75 V, while the valley exhibits at much lower potential. The anodic peaks in the following

cycles locate at around 0.8 V, which is realized as the reversible electrochemical potential for Fe_2O_3 and Fe_3O_4 [40,41]. After the first cycle of sweep, all the single crystal nanowires are converted to nanocrystals within the range of nanowire frame, according to our previous results. It is likely attributed to the much more polarized peak in the first cycle, since certain amount of energy is required to overcome phase transformation from single crystal to nanocrystals. It is worth noting that, regardless of the cycles, all the cathodic peaks exhibits much broader width than those of the anodic peaks, indicating a sluggish re-oxidation process for Fe_xO_y nanowires during delithiation. The voltage hysteresis ($\Delta E_{hys} = E_{cath} - E_{anod}$) of our samples are smaller than other reported 1 and 1.6 V [38,52], which could be due to the suppressed contact resistance of directly grown nanowires [48]. It is widely known that the surface modification with carbonous material enhances the electron migration in the reaction, resulting in the suppressed polarization and life span improvement. In our results, during 15 cycles of swept, α-Fe_2O_3-C nanowires show much better reversibility in terms of the current retention than α-Fe_2O_3. Moreover, we find out that Fe_3O_4-C exhibits slightly better cycle performance than α-Fe_2O_3-C, and optimized reaction kinetics associated with Li, since the anodic peaks present narrower half-peak width and more consistent position. It is likely caused by the improved electronic conductivity of Fe_3O_4 ($\sigma \sim 10^{-2}$ S/m) rather than α-Fe_2O_3 ($\sigma \sim 10^{-8}$ S/m) at room temperature [53,54]. Therefore, Fe_3O_4 can be realized as the most promising electrode materials in the Fe_xO_y category based on our CV results.

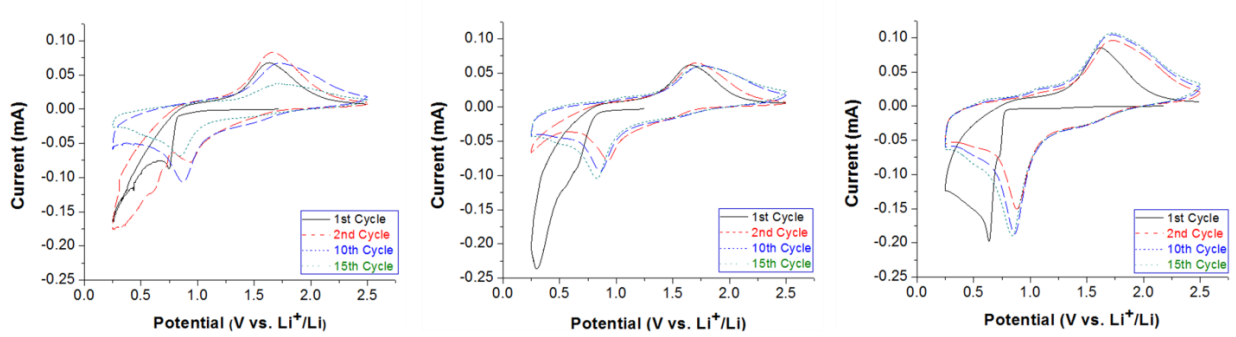

Figure 3.2 Cyclic voltammagrams of nanowires cycled against Li metal at scan rates of 500 μV/s: α-Fe_2O_3 (a), α-Fe_2O_3-C (b) and Fe_3O_4-C (c).

Figure 3.3 describes the rate capacity and columbic efficiency of Fe_3O_4 nanowires array cycled against Li. In the first 5 cycles, the efficiency keeps increasing from 60% to 96%, with certain irreversible capacity. The suggested reasons could be: (1) solid electrolyte interface (SEI) formation on the large surface area of nanowire array; (b) lithium intercalation into irreversible sites in the crystal structure; (c) side reaction from the absorbed species containing H_2O, O_2, etc. [48] P. L. Taberna et al. has electrochemically deposited Fe_3O_4 nano-particle on the copper array, achieving high energy density of 0.35 mAh/cm^2 at low rate discharge [37]. However, our sample advanced the energy density up to 1.1 mAh/cm^2, which could potentially attract commercial interest. At various current densities, the capacity retention is reasonable as well as the columbic efficiency when the rate increases 8 times.

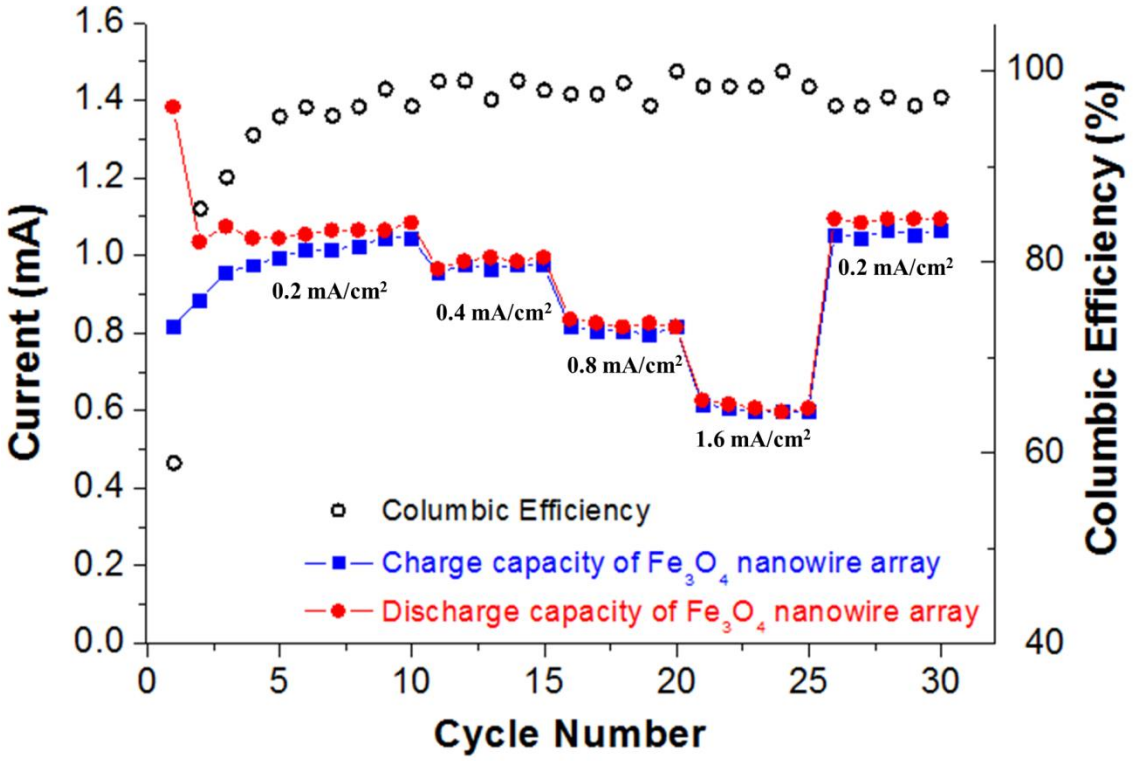

Figure 3.3 Rate performance and columbic efficiency of Fe_3O_4 nanowire array against Li at various current density.

Reference

[1] R. Vasant Kumar, T. Sarakonsri, High Energy Density Lithium Batteries, (2010) 1.

[2] A. Manthiram, T. Muraliganth, Handbook of Battery, (2011) 345.

[3] "DoITPoMS Teaching and Learning Packages," University of Cambridge, 2005. [Online]. Available: http://www.doitpoms.ac.uk/tlplib/batteries/index.php. [Accessed 5 February 2010].

[4] G. Pistoia, Battery Operated Devices and Systems, (2008) 321.

[5] B. Dunn, H. Kamath, J-M. Tarascon, Science, 18 (2011) 928.

[6] M.R. Palacin, Chemical Society Reviews, 38 (2009) 2565.

[7] K. Mizushima, P.C. Jones, P.J. Wiseman, J.B. Goodenough, Materials Research Bulletin, 15 (1980) 783-789.

[8] J. Cabana, L. Monconduit, D. Larcher, M.R. Palacin, Advanced Materials, 22 (2010) E170.

[9] J. Jiang, Y. Li, J. Liu, X. Huang, C. Yuan, X.W. Lou, Advanced Materials, 24 (2012) 5166.

[10] P. Poizot, S. Laruelle, S. Grugeon, L. Dupont, J-M. Tarascon, Nature, 407 (2000) 496.

[11] J. B. Goodenough, Y. Kim, Chemistry of Materials. 22 (2010) 587.

[12] M. Ogasa, IEEJ Trans. Electr. Electron. Eng. 3 (2008) 15.

[13] P. Poizot, S. Laruelle, S. Grugeon, L. Dupont, J-M. Tarascon, Nature, 407 (2000) 496.

[14] S.U. M. Khan, J. Akikusa, Journal of Chemical Physics, 103 (1999) 7184.

[15] Z. Yang, J. Zhang, M. C. Meyer, X. Lu, D. W. Choi, J. P. Lemmon, J. Liu, Chemical Reviews, 111 (2011) 3577.

[16] C. Daniel, JOM 60 (2008) 43.

[17] A.K. Shukla, T.P. Kumar, Current Science, 94 (2008) 314.

[18] D. Larcher, C. Masquelier, D. Bonnin, Y. Chabre, V. Masson, J.-B. Leriche, J.-M. Tarascon, Journal of the Electrochemical Society, 150 (2003) 133.

[19] M.V. Reddy, T. Yu, C.-H. Sow, Z.X. Shen, C.T. Lim, G.V. Subba Rao, B.V. R. Chowdari, Advanced Functional Materials, 17 (2007) 2792.

[20] J.S. Chen, T. Zhu, X.H. Yang, H.G. Yang, X.W. Lou, Journal of American Chemical Society, vol. 132, pp. 13162-13164, 2010.

[21] Z.Y. Wang, D. Luan, S. Madhavi, Y. Hu, X.W. Lou, Energy & Environmental Science, 5 (2011) 5252.

[22] J. Chen, L. Xu, W. Li, X. Gou, Advanced Materials, 17 (2010) 582.

[23] D. Larchera, C. Masquelier, D. Bonnin, Y. Chabre, V. Masson, J.-B. Leriche, J.-M. Tarascon, Journal of The Electrochemical Society, 1 (2003) 150.

[24] S.Y. Zeng, K.B. Tang, T.W. Li, Z.H. Liang, D. Wang, Y.K. Wang, Y.X. Qi, W.W. Zhou, The Journal of Physical Chemistry, 112 (2008) 4836.

[25] C.Z. Wu, P. Yin, X. Zhu, C.Z. Ouyang, Y. Xie, Journal of Physical Chemistry, 110 (2006) 17806.

[26] J. Chen, L. Xu, W. Li, X. Gou, Advanced Materials, 17 (2005) 582.

[27] H.S. Kim, Y. Piao, S.H. Kang, T. Hyeon, Y.E. Sung, Electrochemistry Communications, 12 (2010) 382.

[28] J.S. Zhou, H.H. Song, X.H. Chen, L.J. Zhi, S.Y. Yang, J.P. Huo, W.T. Yang, Chemistry of Materials, 21 (2009) 2935.

[29] J. Fei, Y. Cui, J. Zhao, L. Gao, Y. Yang, J. Li, Journal of Materials Chemistry, 21 (2011) 11742.

[30] L.S. Zhong, J.S. Hu, H.P. Liang, A.M. Cao, W.G. Song, L.J. Wan, Advanced Materials, 18 (2006) 2426.

[31] W.S. Choi, H.Y. Koo, Z. Zhong, Y. Li, D.Y. Kim, Advanced Functional Materials, 17 (2007) 1743.

[32] Z. Wang, D. Luan, S. Madhavi, C. Ming Li, X.W. Lou, Chemical Communications, 47 (2011) 8061.

[33] E. García-Tamayo, M. Valvo, U. Lafont, C. Locati, D. Munao, E.M. Kelder, Journal of Power Sources, 196 (2011) 6425.

[34] H. Liu, G. Wang, J. Park, J. Wang, H. Liu, C. Zhang, Electrochimica Acta, 54 (2009) 1733.

[35] D. Larchera, D. Bonninb, R. Cortes, I. Rivals, L. Personnaz, J.-M. Tarascon, Journal of the Electrochemical Society, 150 (2003) A1643-A1650.

[36] A.G. Nasibulin, S. Rackauskas, H. Jiang, Y. Tian, P.R. Mudimela, S.D. Shandakov, L. Nasibulina, J. SainioM, E.I. Kauppinen, Nano Research, 2 (2009) 373.

[37] P.L. Taberna, S. Mitra, P. Poizot, P. Simon, J.M. Tarascon, Nature Materials, 5 (2006) 567-573.

[38] D. Larcher, C. Masquelier, D. Bonnin, Y. Chabre, V. Masson, J.B. Leriche, J.M. Tarascon, Journal of the Electrochemical Society, 150 (2003) A133-A139.

[39] H. Liu, G. Wang, J. Park, J. Wang, C. Zhang, Electrochimica Acta, 54 (2009) 1733-1736.

[40] X.L. Wu, Y.G. Guo, L.J. Wan, C.W. Hu, Journal of Physical Chemistry C, 112 (2008) 16824-16829.

[41] Y. NuLi, R. Zeng, P. Zhang, Z. Guo, H. Liu, Journal of Power Sources, 184 (2008) 456-461.

[42] J. Li, H.M. Dahn, L.J. Krause, D.B. Le, J.R. Dahn, Journal of the Electrochemical Society, 155 (2008) A812-A816.

[43] S. Zeng, K. Tang, T. Li, Z. Liang, D. Wang, Y. Wang, W. Zhou, Journal of Physical Chemistry C, 111 (2007) 10217-10225.

[44] P.C. Wang, H.P. Ding, T. Bark, C.H. Chen, Electrochimica Acta, 52 (2007) 6650-6655.

[45] F. Jiao, J. Bao, P.G. Bruce, Electrochemical and Solid-State Letters, 10 (2007) A264-A266.

[46] J. Morales, L. Sánchez, F. Martín, F. Berry, X. Ren, Journal of the Electrochemical Society, 152 (2005) A1748-A1754.

[47] J. Chen, L. Xu, W. Li, X. Gou, Advanced Materials, 17 (2005) 582-586.

[48] H. Han, T. Song, E.K. Lee, A. Devadoss, Y. Jeon, J. Ha, Y.C. Chung, Y.M. Choi, Y.G. Jung, U. Paik, ACS Nano, 6 (2012) 8308-8315.

[49] A.G. Nasibulin, S. Rackauskas, H. Jiang, Y. Tian, P.R. Mudimela, S.D. Shandakov, L.I. Nasibulina, S. Jani, E.I. Kauppinen, Nano Research, 2 (2009) 373-379.

[50] B. Mauvernay, M.L. Doublet, L. Monconduit, Journal of Physics and Chemistry of Solids, V67 (2006) 1252-1257.

[51] H. Kitaura, K. Takahashi, F. Mizuno, A. Hayashi, K. Tadanaga, M. Tatsumisago, Journal of the Electrochemical Society, 154 (2007) A725-A729.

[52] M.V. Reddy, T. Yu, C.H. Sow, Z.X. Shen, C.T. Lim, G.V.S. Rao, B.V.R. Chowdari, Advanced Functional Materials, 17 (2007) 2792-2799.

[53] E.J.W. Verwey, P.W. Haayman, Physica, 8 (1941) 979-987.

[54] S. Ito, Y. Yui, J. Mizuguchi, Materials Transactions, 51 (2010) 1163-1167.